

Simulation of metal additive manufacturing microstructures using kinetic Monte Carlo



Theron M. Rodgers^{a,*}, Jonathan D. Madison^b, Veena Tikare^c

^a Computational Materials & Data Science, Sandia National Laboratories, PO Box 5800 MS-1411, Albuquerque, NM 87185, USA

^b Materials Mechanics, Sandia National Laboratories, PO Box 5800 MS-0889, Albuquerque, NM 87185, USA

^c Multiscale Science, Sandia National Laboratories, PO Box 5800 MS-1321, Albuquerque, NM 87185, USA

ARTICLE INFO

Article history:

Received 20 October 2016

Received in revised form 27 March 2017

Accepted 31 March 2017

Available online 19 April 2017

Keywords:

Kinetic Monte Carlo

Microstructure

Additive manufacturing

ABSTRACT

Additive manufacturing (AM) is of tremendous interest given its ability to realize complex, non-traditional geometries in engineered structural materials. However, microstructures generated from AM processes can be equally, if not more, complex than their conventionally processed counterparts. While some microstructural features observed in AM may also occur in more traditional solidification processes, the introduction of spatially and temporally mobile heat sources can result in significant microstructural heterogeneity. While grain size and shape in metal AM structures are understood to be highly dependent on both local and global temperature profiles, the exact form of this relation is not well understood. Here, an idealized molten zone and temperature-dependent grain boundary mobility are implemented in a kinetic Monte Carlo model to predict three-dimensional grain structure in additively manufactured metals. To demonstrate the flexibility of the model, synthetic microstructures are generated under conditions mimicking relatively diverse experimental results present in the literature. Simulated microstructures are then qualitatively and quantitatively compared to their experimental complements and are shown to be in good agreement.

© 2017 The Authors. Published by Elsevier B.V. This is an open access article under the CC BY license (<http://creativecommons.org/licenses/by/4.0/>).

1. Introduction

1.1. Metal additive manufacturing techniques

Metal additive manufacturing (AM) allows for the creation of non-traditional and highly complex parts with sophisticated geometries [1]. The field is rapidly evolving with significant activity directed toward improving processing methods, understanding material compositions, developing post-build heat treatments, and the computational tools to treat these various aspects [1–4]. Based upon the powder-delivery method, metal additive manufacturing methods can be classified into two general categories: (1) Laser Engineered Net Shaping (LENS) or (2) Powder Bed Fusion (PBF). LENS methods utilize a carrier gas stream to transport powder through a nozzle directly into a melt pool (typically generated by a coaxial laser) at the surface of the build [5]. In PBF, a heat source (typically an electron or laser beam) is rastered across a bed of metallic powder to locally melt and solidify material. Upon completion of a layer, additional powder is spread onto the bed from

an adjacent reservoir [6] and the process continues. Both methods construct builds in a layer-by-layer fashion, but have markedly different melting and solidification dynamics. Raster-patterns in LENS methods are typically less complex than those found in PBF, as the powder nozzle and coaxial laser assembly must move in tandem. Alternatively, PBF techniques, which raster the incident beam with mirrors or electromagnetic fields, are capable of faster scan rates and more elaborate scan strategies [7,8].

1.2. Common features of AM microstructures

While metal additive manufacturing techniques can be generally classified in two categories, the multitude of machines, material systems and specific goals for AM implementation have yielded tremendous variety in microstructures. This drastic variability at the microstructural level is due to the non-uniform local solidification behavior occurring in the process [1,2]. Common features of the resulting heterogeneity are a mixture of elongated and equiaxed grains, often having a visible periodicity corresponding to the layer height, line width and scan pattern used [7,9]. The transition between these grain types is controlled by the thermal gradient (G) and solidification front velocity (V) at the solid-liquid interface. These two parameters have been used to understand

* Corresponding author.

E-mail addresses: trodger@sandia.gov (T.M. Rodgers), jdmadis@sandia.gov (J.D. Madison), vtikare@sandia.gov (V. Tikare).

and predict microstructural morphologies in directional solidification [10] and welding for decades [11,12].

In addition to basic solidification behavior, the varying scan patterns for PBF and LENS methods have also been shown to produce significant changes in grain structure [7,9]. Island scan strategies in PBF (where the build layer is divided into independently-scanned sub-regions) can lead to rectangular partitions of elongated grains bound by equiaxed microstructures [7]. Linear scan patterns in LENS can lead to more continuous grain structures along the scan direction [13]. Furthermore, simple variations such as scanning in a uni- or bi-directional pattern, or cross-hatching between layers can also lead to additional variation in resulting grain morphology [9,14]. These deviations from microstructures created by traditional techniques can result in varied mechanical properties [15–17]. The variation across such an extensive and sensitive set of processing parameters makes the use of traditional design of experiment approaches both expensive and time consuming. However, the use of process modeling and subsequent data science based analyses offer a significant opportunity for the acceleration of process development and microstructural forecasting in the realm of AM [18].

1.3. Applications of computational materials science to AM

Current models for microstructure prediction in additive manufacturing are often extensions of methods initially developed for directional solidification or welding [19]. A number of these have included coupled cellular automata-finite element (CAFE) [20–24] or Lattice Boltzmann-cellular automata approaches [25,26]. The cellular automata models were designed for a single solidification front with limited effects from subsequent reheating or remelting. Additionally, while these methods often simulate grain growth with a detailed treatment of solidification, most are currently limited to two-dimensions and/or a relatively restrictive number of heat source passes in comparison to an actual additive build. Comparisons of the strengths and weaknesses of these various methods are summarized in Table 1. It is important to note that for current computing capabilities, even “low” cost methods

may remain impractical for microstructural simulations of an entire AM build (especially for powder-bed methods where the cumulative path length of the beam over the entire build process can be many kilometers [4]).

The need for computationally efficient techniques to predict varying characteristics of AM-produced components, at the scale of experimental builds, has been identified by many researchers [3,25,27]. This is a challenge as typical additive manufacturing processes can require solidification of hundreds of layers and hours of build time. Many electron-beam and laser welding models capture relevant physics but are limited to short lengths and/or abbreviated time scales [12,28]. Current literature suggests a number of simulation methods are under active development for either high-fidelity modeling of AM processes at short times and small length scales [27], or conversely, lower-complexity simulations at longer times and greater length scales [29,30]. Regardless, few methods exist that capture fine-scale microstructural detail across a sufficiently large scale to predict microstructure over many passes and layers.

In the 1980s Ashby, Easterling, and Ion proposed a kinetics-based model for the prediction of average grain size in the heat-affected zone (HAZ) of weldments using a formalization of stochastic probability [32,33]. This model argued that curvature-driven grain growth within a thermal gradient was the dominant mechanism for grain evolution. The kinetic model used closely resembles the integration of the Metropolis function (commonly used in many Monte Carlo simulation techniques) over the temperature history present. Recently, Wang, Palmer, and Beese extended the model to predict average grain size in AM microstructures [15]. Although the mechanism of grain nucleation from the molten zone has yet to be robustly treated in models of this fidelity, these works show significant portions of grain formation can be reliably described by the treatment of grain boundary curvature as a primary mechanism.

In this work, a similar approach is invoked for the simulation of grain evolution over hundreds of passes in a 3D domain. The method is derived from the Potts kinetic Monte Carlo model for grain growth [34] and builds upon recent modifications to enable

Table 1
Comparison of AM microstructure simulation methods.

Method and Approximate Computational Cost	Benefits	Challenges
Cellular Automata-Finite Element (CAFE) (High) [21,23]	<ul style="list-style-type: none"> Provides coupled predictions of thermal behavior and microstructure. Incorporates crystallographic texture. 	<ul style="list-style-type: none"> Does not simulate solid-state grain evolution after solidification. Limited to few passes of a heat source. Free open-source code currently unavailable.
Cellular Automata-Lattice Boltzmann (High) [26]	<ul style="list-style-type: none"> Allows for coupled thermofluid and microstructure evolution on same lattice. Incorporates crystallographic texture. 	<ul style="list-style-type: none"> Lattice Boltzmann provides unstable solutions for many regimes. Does not simulate solid-state grain evolution after solidification. Limited to few passes of a heat source. Free open-source code currently unavailable.
Monte Carlo (Medium) [18,30]	<ul style="list-style-type: none"> Predicts full 3D microstructures with hundreds of heat source passes. Approximates microstructure during solidification and solid-state grain evolution. Utilizes idealized molten zones, without the need to parameterize for specific material systems. Included in the open-source SPPARKS Monte Carlo suite. 	<ul style="list-style-type: none"> Does not allow for direct coupling of thermal and microstructural models. Quantitative ties to experimental conditions are less developed. Currently does not incorporate material texture or anisotropy.
Empirical Microstructure models (Low if thermal prediction exists, otherwise medium) [31]	<ul style="list-style-type: none"> Estimates microstructural features over large builds. Allows extension of pre-existing thermal simulation models. 	<ul style="list-style-type: none"> Does not provide microstructure for further analysis. Requires estimation of thermal environment. Not well explored for many material systems in AM.

the modeling of grain evolution in electron beam and laser welding [30]. In this paper, the general Potts Monte Carlo approach and modifications to the model for the study of solidification are presented first. The results section then demonstrates the utility of the method by comparing simulated microstructures to experimental results across three additive manufacturing cases and material systems in the literature. Lastly, applications of synthetic microstructures, and potential extensions of the method are discussed.

2. Methods

2.1. The Potts model

Fundamentally, the Monte Carlo Potts model is an on-lattice technique for the simulation of curvature driven grain growth [34]. The method approximates a polycrystalline microstructure by assigning an integer “spin” to each lattice site. Contiguous sites of the same spin compose a grain. Local configurational energy is determined at each lattice site by comparing a site’s spin to that of its neighbors. Neighbors with unlike spins contribute to the system’s total energy, while neighbors with identical spin do not. The total system energy is thus determined by:

$$E = \frac{1}{2} \sum_{i=1}^N \sum_{j=1}^L (1 - \delta(q_i, q_j)) \quad (1)$$

where N is the total number of lattice sites and L is the number of neighbors at each site (where $L = 26$ or 8 in the case of 3D or 2D domains, respectively). The spin at each lattice site is q_i , the spin at each neighboring site is q_j , and the Kronecker delta function is δ , which is equal to 1 when $q_i = q_j$ and 0 otherwise.

System energy is minimized through curvature-driven grain growth where grain evolution occurs by randomly reassigning a

lattice site’s spin to that of an unlike neighboring spin; resulting in a change in the overall system energy. The spin assignment is accepted or rejected using the Metropolis algorithm by comparing a random number uniformly distributed between 0 and 1 to the acceptance probability, P , calculated by:

$$P = \begin{cases} \exp\left(\frac{-\Delta E}{k_B T_s}\right), & \text{if } \Delta E > 0 \\ 1, & \text{if } \Delta E \leq 0 \end{cases} \quad (2)$$

where ΔE is the change in system energy, k_B is the Boltzmann’s constant, and T_s is the simulation background temperature. If the change in spin results in a reduction of system energy, it is accepted. If the change in spin results in an increase in system energy, the change can be accepted if the random number is less than P . Simulation time is expressed in Monte Carlo steps (MCS) where each MCS corresponds to the evaluation of a lattice spin update across all sites within the simulation domain.

2.2. Incorporating solidification and molten zone movement

To simulate additive manufacturing processes, several modifications are made to the standard Potts model. In the approach outlined below, microstructure is evolved only within and immediately outside of the molten zone. This is reasonable as grain growth is not expected in regions far from the molten zone where grain boundary mobility is negligible. While the heat source is not directly simulated, its effect is imposed as a molten zone surrounded by a high-temperature, heat-affected zone (HAZ) having a steep thermal gradient. Together, the molten and heat-affected zones provide the kinetics necessary to enable microstructural evolution. Fig. 1 shows an example molten and heat-affected zone geometry. The molten zone is simulated by assigning spins at random to lattice sites within its boundary. The heat-affected zone surrounding the melt pool governs local grain boundary mobility

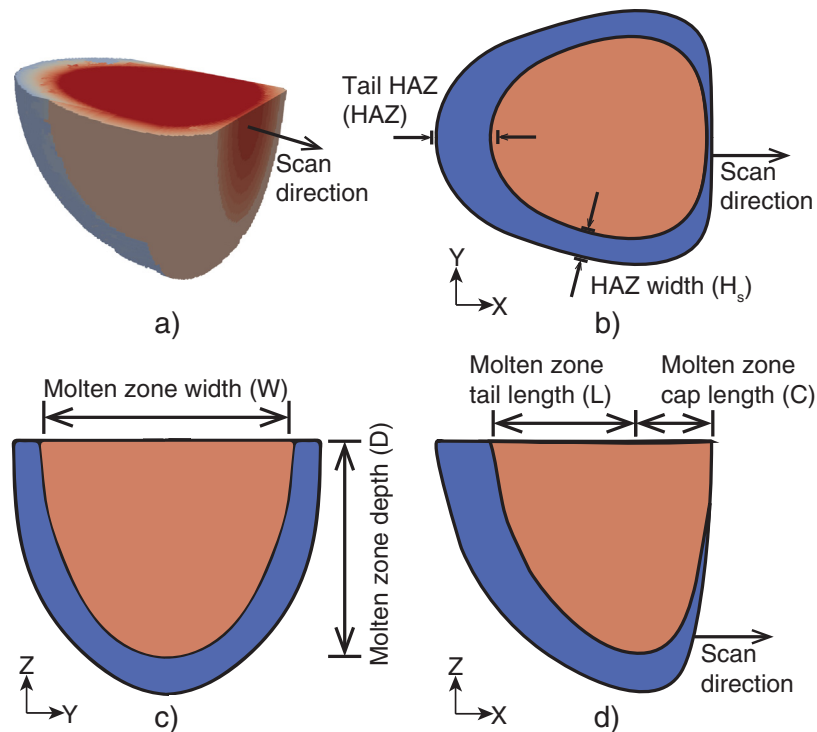


Fig. 1. (a) Idealized 3D molten zone and HAZ with temperature gradient profile used for KMC synthetic microstructure generation. The leading surface is cropped to reveal the temperature gradient in the HAZ. (b–d) Orthogonal cross section schematics of the molten zone and HAZ, molten zone is depicted in orange, and HAZ is shown in blue. (For interpretation of the references to colour in this figure legend, the reader is referred to the web version of this article.)

via an accompanying mobility field described by Equation (3). This mobility has an Arrhenius relationship [35,36] with the local temperature:

$$M(T) = M_0 \exp\left(\frac{-Q}{RT}\right) \quad (3)$$

where Q is the activation energy for grain boundary motion (held constant in this study), M_0 is the Arrhenius pre-factor, R is the gas constant, and T is the local temperature caused by proximity to the solidification boundary. The probability of executing a spin-reassignment for eligible sites then becomes:

$$P = \begin{cases} M(T) \exp\left(\frac{-\Delta E}{k_B T_s}\right), & \text{if } \Delta E > 0 \\ M(T), & \text{if } \Delta E \leq 0 \end{cases} \quad (4)$$

It is important to note that the simulation temperature, T_s , and the physical temperature, T , used to calculate mobility are not the same value. T_s controls the thermal fluctuations in the system [34], while T dictates a local grain boundary mobility. To isolate the effects of mobility $k_B T_s$ is taken to be zero [37].

As the molten zone moves forward, the trailing region solidifies and grains grow quickly as the homologous temperature and grain boundary mobility are both very high. Like the standard Potts model, grains grow by performing Monte Carlo switches with unlike spins of neighboring grains. Spin reassignment can occur with spins of previously-solidified grains (causing grain growth), or among lattice sites that just exited the molten zone (causing grain nucleation). Fig. 2 shows a top-down planar view of the process described above with annotation of the molten zone, solidification boundary, and surrounding HAZ.

2.3. Additive-specific modifications

In the current model, an idealized molten zone and HAZ, are rastered through the simulation domain at a specific build layer. During additive simulations, the molten zone's parameters are held constant. The molten zone's geometry is defined by two coincident ellipsoids that share two axes but have independent lengths along the scan direction. Similar parameters are used to define Goldak's double-ellipsoid heat source model [38]. However, unlike Goldak's model, the current simulation uses a pre-determined molten zone

and HAZ geometry, rather than inputting an energy flux and determining the material response. This approach allows for specification of molten zones with widely varying geometries including long tails and/or abbreviated “caps” as observed in many thermofluid simulations [25,27] without requiring specific knowledge of the material's thermo-fluidic properties. The parameters available for describing the molten zone's geometry are user-defined and are summarized in Table 2. The temperature (and resulting mobility) contours in the HAZ are concentric with the molten zone's boundary. Thus, the temperature gradient is always steepest along the vector normal to the solidification surface.

The characteristics of experimental additively manufactured builds are determined by their beam power, beam focus, spot size, scan rate, and scan pattern with all such parameters playing a vital role in the size and shape of the molten zone and HAZ. Likewise, the user-defined, simulation parameters of Table 2 define the shape and size of the molten and heat-affected zones to provide a simulation surrogate to experimental conditions. The molten zone's depth is dependent on many factors including beam power, spot size and scan rate, while the molten zone's width is highly dependent on beam power and spot size. The molten zone's length is greatly influenced by beam power and scan rate while the HAZ's specifications are highly dependent on the heat dissipation properties of the build configuration and the material's thermal diffusivity.

Remaining modifications required to simulate the multi-pass and multi-layer nature of AM processes include scan pattern details such as cross-hatching, hatch spacing, number of scans per layer, and layer height. These are incorporated into the model as adjustable user inputs. The model incorporates layer remelting and epitaxial growth between layers through adjustment of the molten zone width W , length L , depth D , and HAZ. A snapshot of a molten zone and HAZ traveling through a simulation domain is shown in Fig. 3.

Finally, while the AM process is by definition, “additive”, simulation domains typically do not grow with time. To address this inconsistency, inactive regions are “masked” and evolution of these sites is not allowed prior to initial interaction with the molten zone. This masking does not affect time-evolution of the simulation, which is advanced by a fixed interval each time step. Sites become “unmasked” and evolve when they fall within or below the active build layer. As simulation time progresses, initial spins within each new layer are completely disordered, and non-periodic boundary conditions are used to prevent unphysical interactions at simulation boundaries.

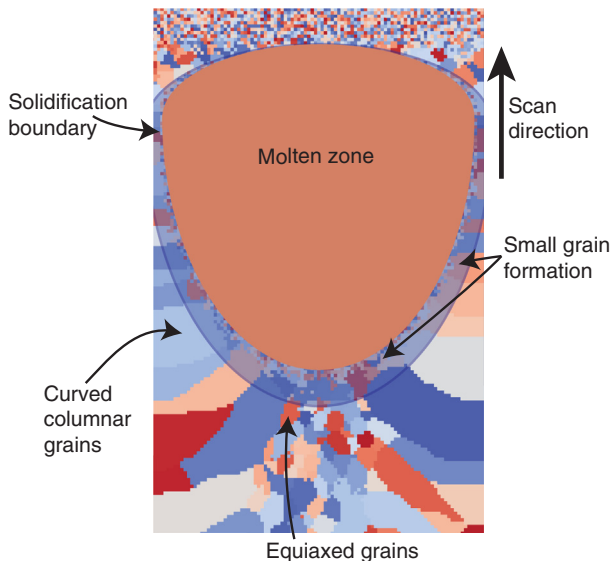


Fig. 2. Top-down view of a molten zone and HAZ traveling through a domain. Small grains just outside the boundary nucleate, but are quickly consumed by much larger grains or coarsen to form larger grains themselves.

Table 2

Molten and heat-affected zone input parameters for simulation. These parameters are also shown schematically in Fig. 1.

Parameter	Description
Molten zone width (W)	Maximum width of molten zone
Molten zone tail length (L)	Maximum length along the scan direction of molten zone's trailing ellipsoid
Molten zone depth (D)	Maximum depth of molten zone
Molten zone cap Length (C)	Maximum length along the scan direction of molten zone's leading ellipsoid
Side HAZ width (H_s)	Width of high-temperature region around molten zone
Tail HAZ width (HAZ)	Length of high-temperature region trailing molten zone
Mobility prefactor (M_0)	Material and process specific parameter that defines the steepness of the mobility gradient in the high-temperature region.
Activation energy (Q)	Material-dependent parameter describing the activation energy for grain boundary motion.

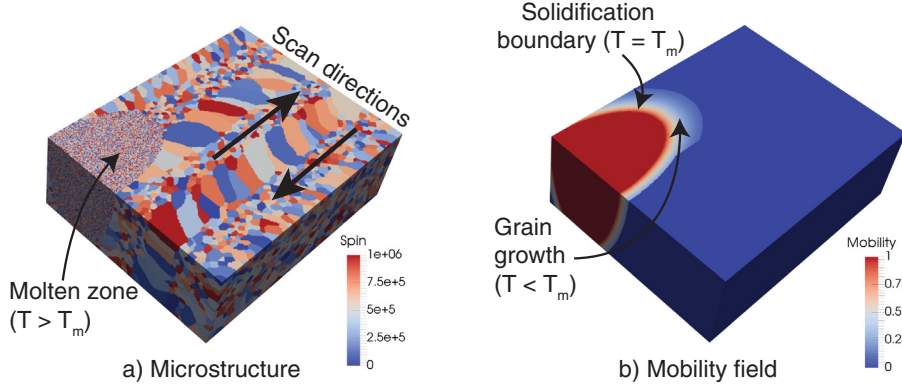


Fig. 3. Schematic of a molten zone and HAZ scanning through a 1-layer thick 3D domain, two rasters in the layer have fully traversed the domain and the third is nearing completion.

2.4. Determining simulation parameters

The KMC model presented, while simple in its implementation, requires understanding in application to such a complex process with several concomitant variables. Experimental AM microstructures result from the convoluted interplay of processing parameters and materials properties as detailed above. Selecting simulation parameters to match experimental variables can be challenging, as decoupling simulation input parameters for any single experiment is not necessarily intuitive. To assist in the selection of appropriate quantities for varying parameters, the authors provide a method to aid in coordinating simulation parameters to experimental variables.

A first step in estimating the proper input parameters can be achieved by integrating the kinetic equations as used by Ion et al. for calculating the microstructural changes in HAZ's of welds [33]. A quantity termed kinetic strength given by:

$$I = \int_0^t e^{-\frac{Q}{RT(i)}} dt \quad (5)$$

is related to the total number of diffusive jumps during the welding cycle. In the model presented in this work, grain boundary mobility incorporates the exponential, which can be expressed as:

$$I = \int_0^t M_0 e^{-\frac{Q}{RT(i)}} dt \quad (6)$$

Here, the kinetic strength, (I), experienced by a lattice site during simulation is ultimately correlated to final grain size within the synthetic microstructure. In many AM simulations, final grain size can be divided into two regimes: large columnar grains spanning multiple build layers (for large I), and smaller equiaxed grains (at small values of I). Due to the discrete nature of the simulation, the integral of Eq. (6) can be calculated by the summation of each site's mobility at every time step:

$$I(i) = \sum_{j=0}^t M(T(i)) \quad (7)$$

where t is the total number of simulation time steps or MCS.

Since mobility is zero outside of the HAZ in the current model, $I(i)$ can be approximated by the total number of time steps the lattice site spends inside the HAZ. Thus, the simulation parameters for HAZ width (HAZ), scan velocity (v), and the amount of overlap between neighboring laser passes and build layers, (O_L), can be used to approximate the kinetic strength of a set of input parameters:

$$I(i) \sim O_L \sum_{j=0}^{\text{HAZ}} M(T(j)) \quad (8)$$

The syntax j/v denotes the summation that occurs with a step size equal to v . Higher velocities result in fewer interactions within the HAZ for each thermal cycle, ultimately resulting in reduced $I(i)$, while larger values of HAZ and O_L increase $I(i)$.

Plots demonstrating the impact of v , O_L , and HAZ are shown in Fig. 4. In Fig. 4(a) HAZ was varied while O_L was held constant at 2. For all conditions, $I(i)$ increases rapidly as v approaches zero and asymptotically approaches zero for large values of v . In Fig. 4 (b) O_L was varied and HAZ was fixed at 90. For cases $O_L = 1, 2$,

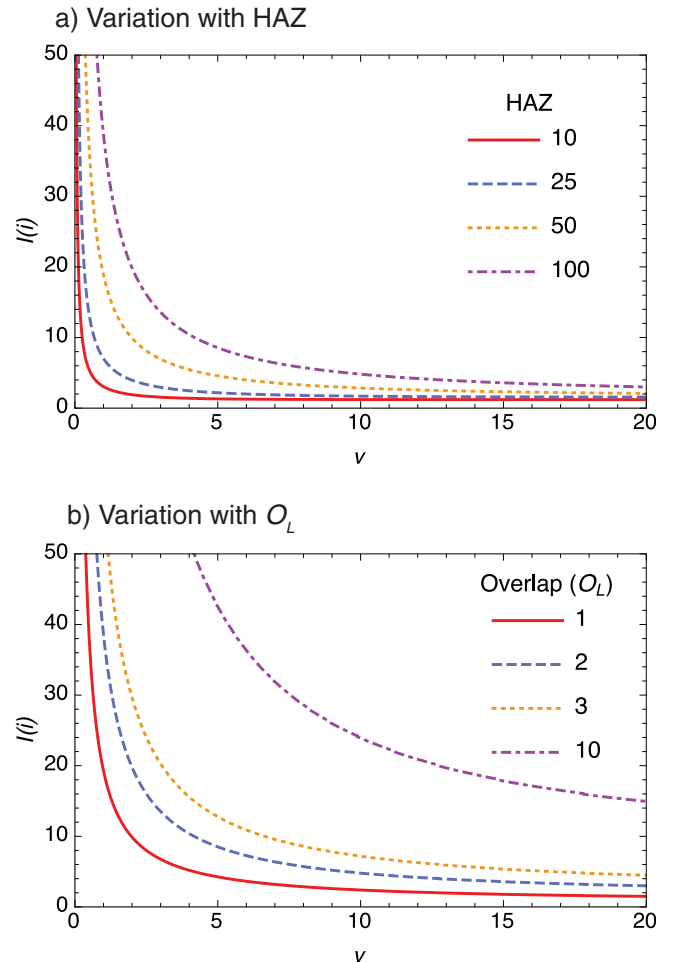


Fig. 4. Plot of $I(i)$ vs velocity for an example temperature profile with varying values of (a) HAZ and (b) O_L . Larger values of $I(i)$ correspond to larger grain sizes.

and 3, a sharp increase in $I(i)$ is observed below a velocity of 3 lattice sites/MCS, which indicates the formation of large grains. The small values of $I(i)$ at high velocities correspond to final microstructures with small, equiaxed grains. For some parameter combinations (e.g. $O_L = 10$), small values of $I(i)$ are unobtainable, as small $I(i)$ will require a v that is too fast. This scenario results in the unphysical condition wherein the molten zone and HAZ travel greater distances during each time step than their physical length, giving rise to a simulation of the molten zone skipping over lattice sites without inducing melting or grain growth. To avoid this, v should be less than HAZ.

Eq. (8) neglects the differing thermal cycles experienced in varying transverse locations within a molten zone's raster path and therefore result in a roughly uniform $I(i)$ throughout the simulation domain. The simplification also neglects the effects of remelting on grain size (previous work shows that the size of re-solidified grains have a near-linear relationship with initial grain size [30]). Furthermore, the authors would add that this formulation is not meant to be a precise or exhaustive prediction of site specific grain size. Rather, this approximation is intended to provide users with two basic items; (1) an estimation tool to forecast what regime of grain size a simulation will yield as a function of its input parameters, and (2) an assessment of the variation that can be expected with parameter modification. With this understanding, a user can then scale their remaining simulation inputs in accordance with their known experimental parameters (or limits) to derive a meaningful simulation of AM synthetic microstructure. A Mathematica notebook which calculates $I(i)$ is included as [supplemental material](#) to this article to assist readers in selecting the most appropriate input parameters for their studies.

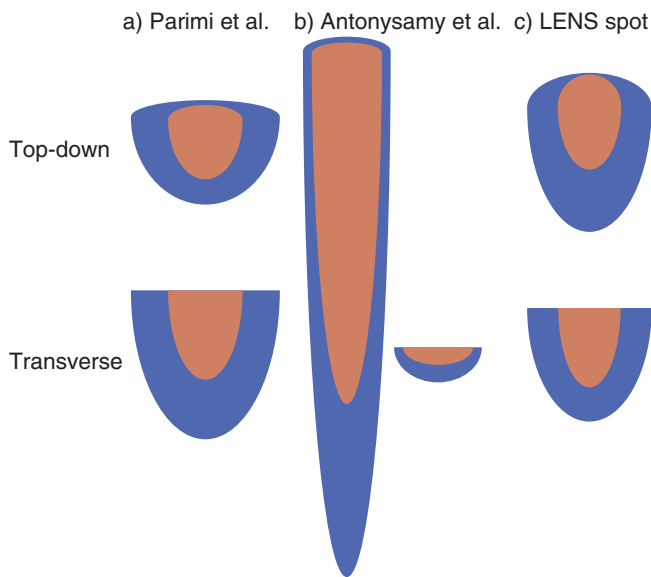


Fig. 5. Schematics of the molten zone and HAZ geometries used in the cases presented in Section 3. These zones are not shown to scale between the three cases.

3. Results

To demonstrate the flexibility of the model, experimental AM studies of various material systems were selected from the literature for comparison. Simulation parameters were calibrated to mimic the experimental conditions as provided in the papers of Parimi et al. [9], Antonyasamy et al. [39], and Nishida et al. [40]. The three molten and heat-affected zone geometries are shown in Fig. 5. The simulated studies of Parimi et al. and Nishida et al. both imitate LENS-like processes, which have globular, loosely symmetric molten zones. The molten zone used to simulate the work of Antonyasamy et al., is indicative of a powder-bed electron beam melting (EBM) process whose molten zone was more shallow and elongated than that of the other two processes. The EBM molten zone had a length-to-width aspect ratio on the order of 5:1 and a length-to-depth aspect ratio on the order of 20:1. The varying molten zone and HAZ geometries of the three examples, along with the diverse scan patterns resulted in tremendous variation in microstructure, as will be demonstrated in the following sections via qualitative and quantitative comparison.

3.1. Columnar and equiaxed microstructures

Widespread observations in AM microstructures have noted the presence of equiaxed, columnar, and mixed grain microstructures [9,13,41,42]. Grains in mixed and equiaxed AM microstructures are typically on the length scale of a deposited layer, while those having columnar microstructures can epitaxially grow over several layers [13,43]. With current AM processes, many routes can exist to create a build. However, these varied processing routes may result in disparate microstructures with corresponding variations in material properties. An example of microstructural sensitivity to processing conditions was shown by Parimi et al. [9]. In their study, grain microstructures across three build conditions using the same metal powders were analyzed and compared. Experimental parameters for each build are shown in Table 3. Additionally, the powder feed rate was reduced in Build 3 to compensate for the increased powder capture efficiency of the larger molten zone. Each processing method produced near fully-dense samples with porosities at or below 1%.

3.1.1. Qualitative comparison

EBSID images of the resulting experimental microstructures are shown in the top row of Fig. 6. Large differences in grain size distribution and morphologies are apparent with changing process parameters. The corresponding simulated microstructures are shown in the bottom row of Fig. 6. For both experiment and simulation, identical processing conditions were used in Builds 1 and 2 with exception to the scan pattern. Build 1 was created by rastering only from right to left and resulted in a layer-wise structure with elongated grains inclined along the raster direction. Build 2 utilized a pattern that rastered in alternating directions with each successive build layer. This resulted in a “zig-zag” microstructure with grain inclinations alternating with each layer [9]. The simu-

Table 3

Experimental parameters used in Ref. [9] along with representative simulation conditions. All simulation parameters are in lattice sites.

		Build 1	Build 2	Build 3
Experiment [9]	Raster pattern	Unidirectional	Bi-directional	Bi-directional
	Power	390 W	390 W	900 W
	Laser operation	6 s pause between scans	Continuous	Continuous
Simulation	Molten zone width (lattice sites)	100	100	175
	Molten zone depth (lattice sites)	120	120	325
	Molten zone tail length (lattice sites)	80	80	450
	HAZ width (lattice sites)	50	50	212

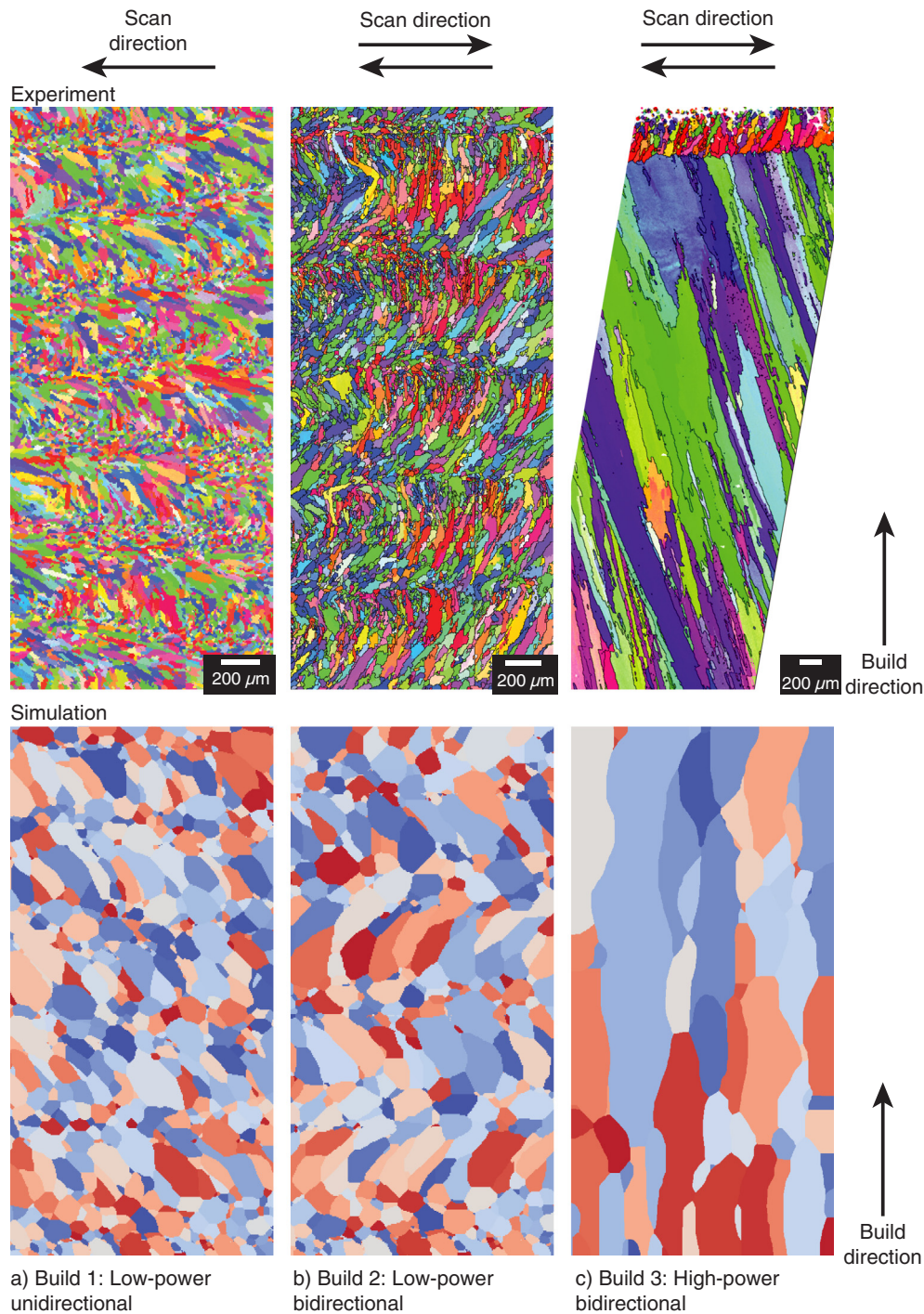


Fig. 6. Cross sections showing microstructures of AM builds from the work of Parimi et al [9], and of simulated AM builds that matched the conditions of Parimi et al., as given by Table 3. Builds 1 and 2 (a and b) use identical conditions but different scan conditions. Build 3 uses much higher beam power (c). Color in the experimental images corresponds to grain orientation, while colors in the simulations are only used to differentiate between grains. (For interpretation of the references to colour in this figure legend, the reader is referred to the web version of this article.)

lated molten zone and HAZ parameters were estimated based on these changes in experimental processing parameters. It was posited that an increasing power and decreasing powder feed rate (as in Build 3) would result in larger molten and heat-affected zones as well as greater remelting between layers. These assumptions were used along with the integral mobility calculation of Section 2.4 to guide selection of simulation parameters resulting in the desired grain size for each condition.

Build 3 used a lower powder feed rate and a higher beam power than Builds 1 and 2. Both factors increase the amount of remelting of previously deposited layers. In Build 3, the layer-by-layer microstructures apparent in Builds 1 and 2 are replaced with elongated grains that span several layers in height. The columnar grains of experimental Build 3 also have a tilt angle of $\sim 10^\circ$ from the surface normal. As explained in [9], this tilt results from a global temperature gradient occurring between the center and edges of each

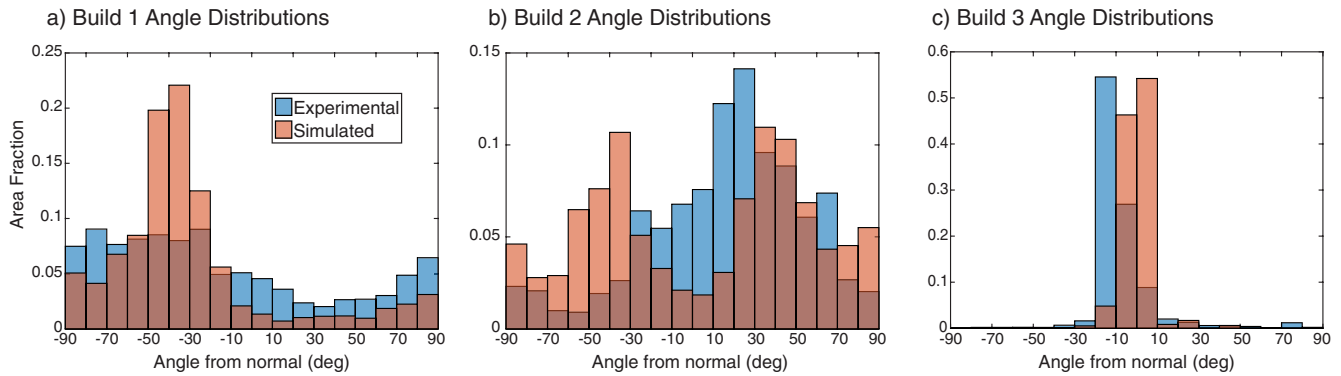


Fig. 7. Comparison of primary grain axis orientations for the three experimental and simulated processing conditions shown in Fig. 6. The histogram bars are transparent to show data in overlapping plot regions.

pass. This long range, residual thermal accumulation is not currently implemented in the model and the lack of global grain inclination in Fig. 6 is indicative of this.

3.1.2. Quantitative comparison

A quantitative comparison between the experimental and simulated grain inclination angles was also performed. The experimental EBSD images were first segmented into grains using the FIJI image analysis package [44]. The experimental and simulated cross sections were then analyzed using Dream3D [45] by fitting each individual grain with an ellipse, and assigning major and minor axes to each ellipse. The angle of inclination of each grain's major-axis was measured with respect to the build direction indicated in Fig. 6. The resulting distributions are then plotted in Fig. 7 for each of the experimental and simulated builds. Grains tilted clockwise have a positive angle, while those tilted counter-clockwise are negative. The histograms were normalized by the total area of each cross section so that the height of each bar represents the fraction of cross sectional area with grains at a given inclination angle.

Each distribution for Build 1 shown in Fig. 7(a) had a center of mass near -40° . The simulated inclination angle distributions generally possessed a narrower and more pronounced peak in their distributions than the experimental results. For Build 2, the simulated distribution shows two maximums corresponding to the zig-zag microstructure, but the experimental results show a more skewed result with most grains oriented in the positive direction. This corresponds to the EBSD maps, as grains tilted in the negative direction are smaller and more random than those in the positive direction. Both the experimental and simulated results for Build 3 (shown in Fig. 7(c)) have a rather narrow distribution centered near the substrate's normal.

3.2. Spatially heterogeneous microstructures

In addition to microstructural variation with processing parameters, significant spatially-correlated variation can result from very simple scan strategies. This is demonstrated by the work of Antonysamy et al. in their study of thin wall builds of Ti-6Al-4V built by powder-bed EBM [39]. The experimental and corresponding simulation conditions are listed in Table 4. It should be mentioned that the scan rate and beam power varied during the experiment to prevent additional heat input in the corners of the build.

3.2.1. Qualitative comparison

Experimentally, the build was created using two parallel “contour” passes spaced 0.5 mm apart, resulting in a 50% lateral overlap

Table 4

EBM processing conditions.

Parameter	Experiment [39]	Simulation
Scan rate	0.15–0.3 m/s	75 lattice sites/MCS
Layer height	100 μm	50 lattice sites
Spot size	200 μm	200 \times 1000 (W \times L) lattice sites
Hatch spacing	0.5 mm	75 lattice sites
Scan direction	$\pm X$	$\pm X$

between the two. This pattern resulted in three classes of grain morphology depending on location within the build: (1) small, curved columnar grains (at the outer surfaces of the wall), (2) thin, axial grains (at the center of each scan), and (3) large, columnar grains in the central region of overlap. These grain-types are shown in cross section perpendicular to the scan direction in Fig. 8(a) and in a top-down cross section (normal to the build direction) in Fig. 8(b). Unlike microstructures resulting from shorter molten zones (as in Figs. 6 and 10), grains are not elongated or curved in the scanning direction.

3.2.2. Quantitative comparison

It is apparent from Fig. 8 that the thin walled microstructure is highly spatially dependent. To help quantify this spatial variation, the transverse cross sections in Fig. 8(a) were again analyzed in Dream3D. The simulated and experimental microstructures were segmented into thirds along the Y-axis. Grains were then binned into each third according to the Y-value of their centroid. The distributions of grain inclination angles were then determined within each interval and are shown in Fig. 9. The Y-axis in Fig. 9 corresponds to the fraction of grains belonging to each interval, rather than the area fraction. The experimental results in Fig. 9(a) indicate that grains within the left and right regions are inclined toward the center of the cross section with distribution peaks around 30° and -35° respectively. The distribution in the central region is much narrower and centered near 0° . The corresponding simulation distributions are shown in Fig. 9(b) and reveal a similar trend. The left region's distribution was centered at 15° , while the right region's distribution was centered near -20° . The distributions in the central region also show good agreement, with a tight cluster near 0° .

3.3. Orthogonally anisotropic microstructures

LENS methods have much larger layer heights (~ 0.25 – 1 mm) than those typically found in powder bed fusion processes (~ 10 – 50 μm). The large layer heights allow for the growth of grains with

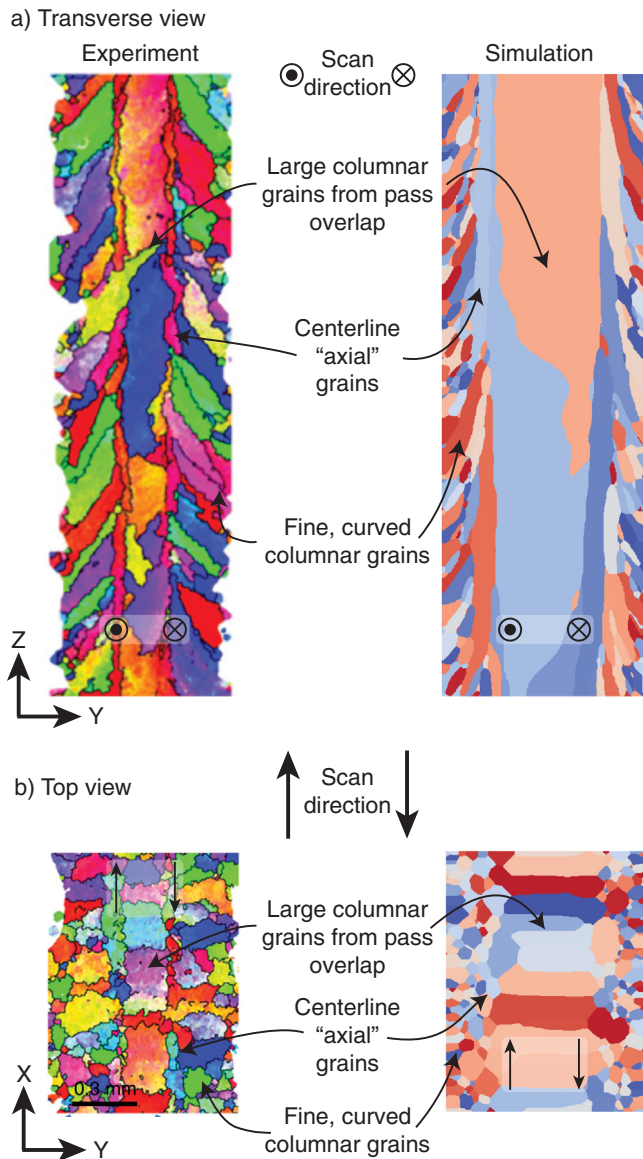


Fig. 8. Image of large cross-layer grains of a two-pass per layer thin wall build as in Antonyasamy et al. [39] (a) Transverse view, (b) Top view. Experimental EBSD images are shown on the left, with the corresponding simulation images on the right.

strongly anisotropic shapes within a single layer. A rectangular brick of 304L stainless steel was deposited using LENS [40] under similar conditions to those described in Carroll et al. [13] by utilizing a defocused, high power laser beam, rastered back and forth along the sample's X-axis. The pertinent experimental and simulation processing conditions are summarized in Table 5.

3.3.1. Qualitative comparison

Experimental and simulated images from three orthogonal planes are shown in Fig. 10. The scan pattern is apparent in the grain structure of the XY, YZ and XZ planes. In the XY plane, the microstructure alternates between fine grains at the center of each pass with larger, transversely elongated grains between them. The multiple-pass structure is also apparent on the YZ plane, which shows a transverse view of three passes. Vertically oriented grains are found at the center of each pass with curved grains between them. The cross section of the XZ plane shows the layer-by-layer microstructure with alternating regions of vertically elongated

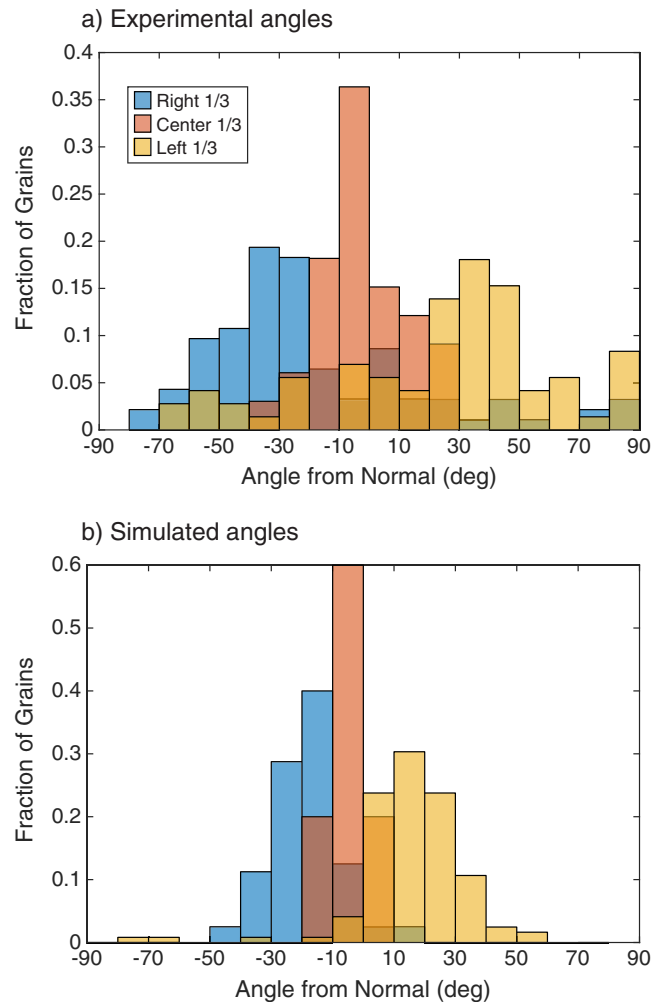


Fig. 9. Primary axis orientation angles for grains within the (a) experimental and (b) simulated cross sections. Each color represents the distribution of angles within the specified interval of the Y-axis. (For interpretation of the references to colour in this figure legend, the reader is referred to the web version of this article.)

grains inclined toward the scan direction. These are bound by alternating layers of equiaxed grains. Additionally, the simulated grain structure reveals a varying grain morphology along the XZ plane depending on the Y-coordinate of the cross section. The XZ images in Fig. 10 were taken from the center line of a beam pass. At cross sections away from the pass's center line, grains become increasingly equiaxed, show a reduction in elongation and a lack of definition between deposition layers.

3.3.2. Quantitative comparison

Since experimental microstructures along all three orthogonal directions were obtained, directionally-dependent quantitative comparisons of the experiment and simulation results are possible. Fig. 11(a) shows histograms of 2D aspect ratios for grains within the experimental microstructures across the three orthogonal planes shown in Fig. 10. Aspect ratios near one represent near-circular grain cross sections, while ratios near 0 represent needle-like cross sections. On the XY plane, the distribution's peak is found near 0.25, indicating a large fraction of elongated grains. The experimental distributions for the YZ and XZ plane are quite similar. Both distributions are broad and center roughly around a value of 0.5 with the XZ distribution having a slight shift toward larger ratios.

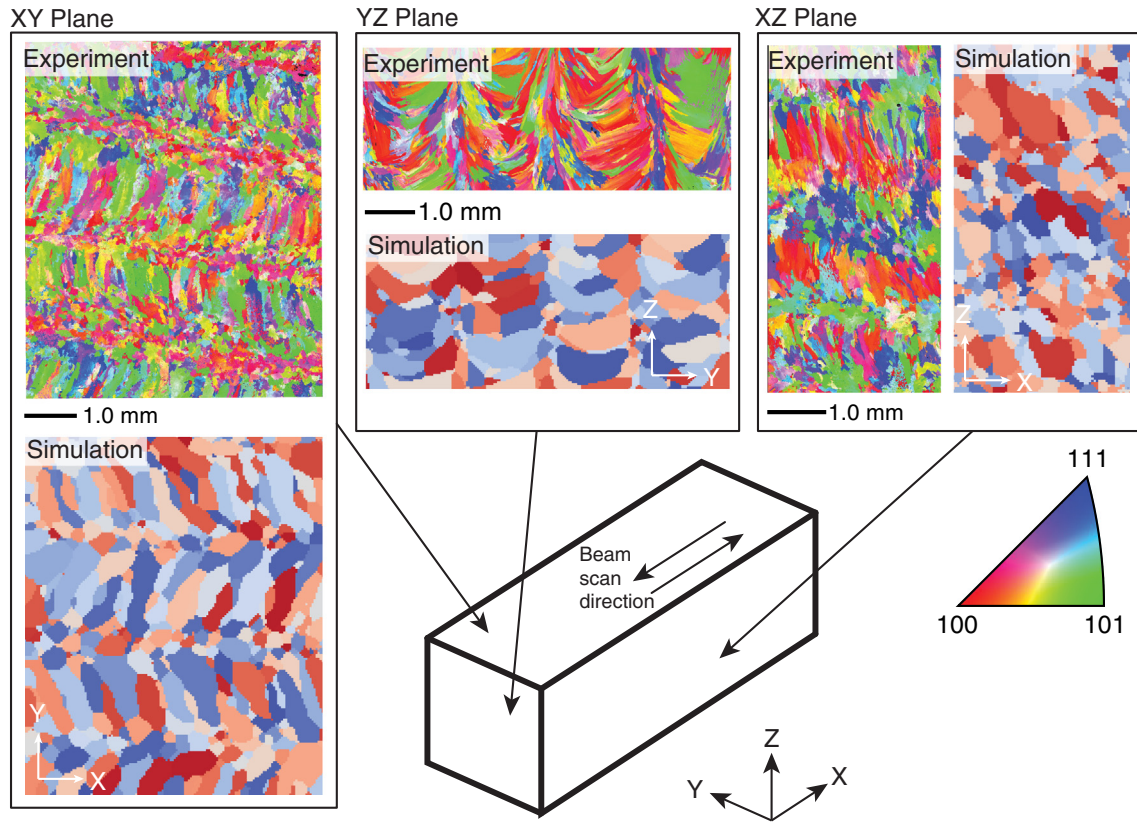


Fig. 10. Comparison between experimental and simulated additively manufactured microstructures along orthogonal planes.

Table 5
LENS processing parameters.

Parameter	Experiment	Simulation
Scan rate	10.58 mm/s	10 lattice sites/MCS
Layer height	1.25 mm	85 lattice sites
Spot size	4 mm	52×51 (W \times L) lattice sites
Hatch spacing	2 mm	50 lattice sites
Scan direction	$\pm X$	$\pm X$

Fig. 11(b) shows the corresponding aspect ratio distributions for the simulated microstructures. In both experiment and simulation, grains on the XY plane are the most elongated with a peak near 0.25. Experiment and simulation also reasonably agree on the YZ plane, as both are centered near 0.5. Along the XZ plane, simulated grains are considerably more isotropic than those observed in the experiment. As in previous comparisons, simulation distributions are typically narrower than those measured in experiment. This difference is likely due to the smaller total quantity of grains in simulation compared with those found in experiment. Additionally, added uncertainty from the EBSD segmentation analysis may also contribute to broadened distributions in the experimental data.

4. Discussion

4.1. Benefits of synthetic microstructures for AM

The strength of the method presented here is its ability to efficiently create 3D synthetic microstructures over large regions consisting of several passes and layers with parameters analogous to experimental processing conditions. This approach makes rapid

analysis of microstructural variation within process parameter space rather tractable. This is exceedingly important in AM as parameters vary both globally with machine inputs and locally with build geometry. In this way, the simulation tool presented, can enable near build-scale simulations to investigate the impact of processing parameter and scan pattern on resulting microstructure. Additionally, for even larger builds, simulations can be performed to explore how local variations in molten and heat-affected zones within a specific region impact the local microstructure.

Once generated, synthetic AM microstructures can be utilized in a variety of ways. The generated microstructures can find use in simulations of material performance (e.g. material mechanics, conductivity, further interrogation of grain morphology, etc.) [4,46], or as initial states for post-processing simulations (e.g. recrystallization and grain growth during subsequent heat treatments or forming processes [47–49]). Additionally, 3D microstructures can provide for multidimensional analysis and correlation development with process or performance metrics which is a difficult task to achieve by experimental means alone [18].

4.2. Model limitations and suggestions for future work

The method presented here makes many simplifying assumptions for the AM process to enable efficient simulation. The model uses predetermined, idealized steady-state molten and heat-affected zones rather than a coupled thermo-fluidic model having a dynamic molten zone. Additionally, the current method does not treat two phase solidification which can be important in many material systems, including Ti-6Al-4V, which often solidifies with a microstructure comprised of α - and β -phase lathes enclosed within larger prior β -grains [16,31,50]. Also, the current model does not include crystallographic orientation among its grains,

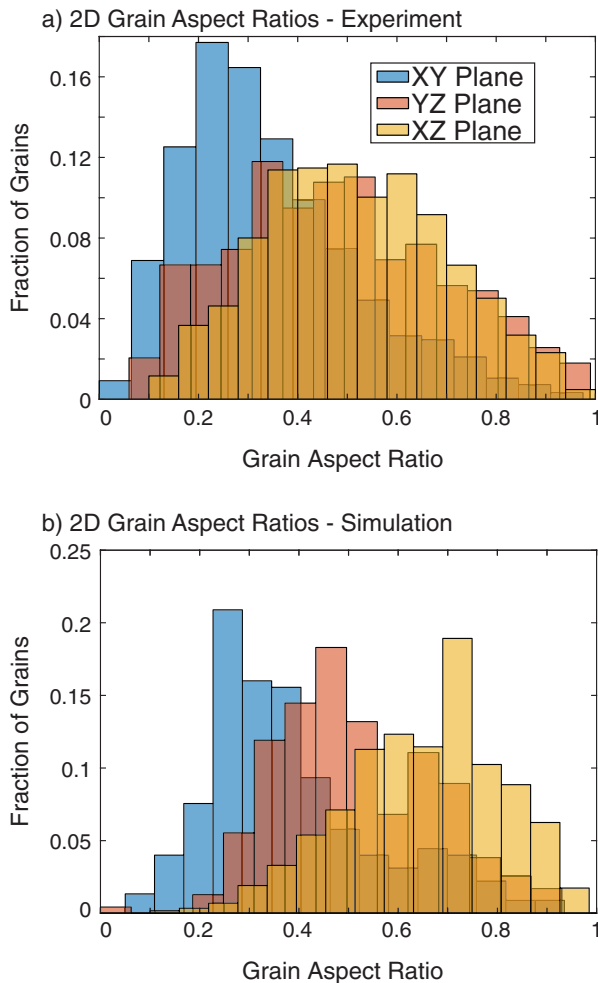


Fig. 11. (a) Experimental and (b) simulated 2D grain aspect ratios.

which can be of significant importance in as-built parts having preferential heat conduction and preferred growth orientations [41,51]. Another limitation is that the modified KMC method presented here does not treat impacts caused by boundary conditions or global deformations. For example, since part geometry is fixed by the simulation domain, the model does not recreate temperature-induced slumping, residual stresses or collapses of overhangs. Lastly, the current simulation model does not consider long-range effects. Meaning, the model does not treat temperature accumulation through the course of the build, which can be significant during the creation of thin walled structures or AM methods requiring significant preheating of the powder bed (as in the case of Ni-based superalloys) [15,41]. Model developments to eliminate these enabling assumptions would increase the effectiveness of the simulation tool and its predictions in future use.

5. Conclusions

A novel simulation technique based on a modified Kinetic Monte Carlo Potts model has been developed to simulate the as-processed microstructure present in additively manufactured metals. The model uses the shape of the molten zone, the surrounding temperature gradient, and the scan pattern to model microstructural evolution. The model's flexibility, in addition to its minimal computational requirements, provide an excellent technique to evaluate grain structure associated with processing-parameter

space for metal additive manufacturing. In this paper, the model was shown to reproduce distinct and varied classes of AM microstructures reported in the open literature and does so with reasonable qualitative and quantitative agreement.

Acknowledgements

The AM model described here is part of the open-source SPPARKS distribution, available for download at <http://spparks.sandia.gov>. The authors would like to thank M.M. Attallah for providing high resolution EBSD maps from Reference 9. Sandia National Laboratories is a multi-mission laboratory managed and operated by Sandia Corporation, a wholly owned subsidiary of Lockheed Martin Corporation, for the U.S. Department of Energy's National Nuclear Security Administration under contract DE-AC04-94AL85000.

Appendix A. Supplementary material

Supplementary data associated with this article can be found, in the online version, at <http://dx.doi.org/10.1016/j.commatsci.2017.03.053>.

References

- [1] W.J. Sames, F.A. List, S. Pannala, R.R. Dehoff, S.S. Babu, The metallurgy and processing science of metal additive manufacturing, *Int. Mater. Rev.* (2016) 1–46.
- [2] W.E. Frazier, Metal additive manufacturing: a review, *J. Mater. Eng. Perform.* 23 (2014) 1917–1928.
- [3] M. Seifi, A. Salem, J. Beuth, O. Harrysson, J.J. Lewandowski, Overview of materials qualification needs for metal additive manufacturing, *JOM* 68 (2016) 747–764.
- [4] M.M. Francois, A. Sun, W.E. King, N.J. Henson, D. Tourret, C.A. Bronkhorst, N.N. Carlson, C.K. Newman, T. Haut, J. Bakosi, J.W. Gibbs, V. Livescu, S.A. Vander Wiel, A.J. Clarke, M.W. Schraad, T. Blacker, H. Lim, T. Rodgers, S. Owen, F. Abdeljawad, J. Madison, A.T. Anderson, J.L. Fattebert, R.M. Ferencz, N.E. Hodge, S.A. Khairallah, O. Walton, Modeling of additive manufacturing processes for metals: Challenges and opportunities, *Curr. Opin. Solid State Mater. Sci.* (2017).
- [5] D.M. Keicher, J.E. Smugeresky, J.A. Romero, M.L. Griffith, L.D. Harwell, in: *Proc. SPIE* 2993, 1997.
- [6] J.P. Kruth, G. Levy, F. Klocke, T.H.C. Childs, Consolidation phenomena in laser and powder-bed based layered manufacturing, *CIRP Ann. – Manuf. Technol.* 56 (2007) 730–759.
- [7] L.N. Carter, C. Martin, P.J. Withers, M.M. Attallah, The influence of the laser scan strategy on grain structure and cracking behaviour in SLM powder-bed fabricated nickel superalloy, *J. Alloy. Compd.* 615 (2014) 338–347.
- [8] N. Raghavan, R. Dehoff, S. Pannala, S. Simunovic, M. Kirka, J. Turner, N. Carlson, S.S. Babu, Numerical modeling of heat-transfer and the influence of process parameters on tailoring the grain morphology of IN718 in electron beam additive manufacturing, *Acta Mater.* 112 (2016) 303–314.
- [9] L.L. Parimi, G.A. Ravi, D. Clark, M.M. Attallah, Microstructural and texture development in direct laser fabricated IN718, *Mater. Charact.* 89 (2014) 102–111.
- [10] M.C. Flemings, Solidification processing, *Metall. Trans.* 5 (1974) 2121–2134.
- [11] S.A. David, J.M. Vitek, Correlation between solidification parameters and weld microstructures, *Int. Mater. Rev.* 34 (1989) 213–245.
- [12] H.L. Wei, J.W. Elmer, T. DebRoy, Origin of grain orientation during solidification of an aluminum alloy, *Acta Mater.* 115 (2016) 123–131.
- [13] B.E. Carroll, T.A. Palmer, A.M. Beese, Anisotropic tensile behavior of Ti-6Al-4V components fabricated with directed energy deposition additive manufacturing, *Acta Mater.* 87 (2015) 309–320.
- [14] H.L. Wei, J. Mazumder, T. DebRoy, Evolution of solidification texture during additive manufacturing, *Sci. Rep.* 5 (2015) 16446.
- [15] Z. Wang, T.A. Palmer, A.M. Beese, Effect of processing parameters on microstructure and tensile properties of austenitic stainless steel 304L made by directed energy deposition additive manufacturing, *Acta Mater.* 110 (2016) 226–235.
- [16] A.M. Beese, B.E. Carroll, Review of mechanical properties of Ti-6Al-4V made by laser-based additive manufacturing using powder feedstock, *JOM* 68 (2015) 724–734.
- [17] B.C. Salzbrener, J.M. Rodelas, J.D. Madison, B.H. Jared, L.P. Swiler, Y.L. Shen, B. L. Boyce, High-throughput stochastic tensile performance of additively manufactured stainless steel, *J. Mater. Process. Technol.* 241 (2017) 1–12.
- [18] E. Popova, T.M. Rodgers, X. Gong, A. Cecen, J.D. Madison, S.R. Kalidindi, Process-structure linkages using a data science approach: application to simulated additive manufacturing data, *Integr. Mater. Manuf. Innov.* (2017).

- [19] H.L. Wei, J.W. Elmer, T. DebRoy, Three-dimensional modeling of grain structure evolution during welding of an aluminum alloy, *Acta Mater.* 126 (2017) 413–425.
- [20] J. Zhang, F.W. Liou, W. Seufzer, J. Newkirk, Z. Fan, H. Liu, T.E. Sparks, in: *Solid Freeform Frabrication Symposium*, Ausin, TX, 2013, pp. 739–748.
- [21] C.A. Gandin, J.L. Desbiolles, M. Rappaz, P. Thevoz, A three-dimensional cellular automaton-finite element model for the prediction of solidification grain structures, *Metall. Mater. Trans. A-Phys. Metall. Mater. Sci.* 30 (1999) 3153–3165.
- [22] C.A. Gandin, T. Carozzani, H. Dignonnet, S. Chen, G. Guillemot, Direct modeling of structures and segregations up to industrial casting scales, *JOM* 65 (2013) 1122–1130.
- [23] A. Zinoviev, O. Zinovieva, V. Ploshikhin, V. Romanova, R. Balokhonov, Evolution of grain structure during laser additive manufacturing. Simulation by a cellular automata method, *Mater. Des.* (2016).
- [24] W. Tan, Y.C. Shin, Multi-scale modeling of solidification and microstructure development in laser keyhole welding process for austenitic stainless steel, *Comput. Mater. Sci.* 98 (2015) 446–458.
- [25] M. Markl, C. Körner, Multiscale modeling of powder bed-based additive manufacturing, *Annu. Rev. Mater. Res.* 46 (2016).
- [26] A. Rai, M. Markl, C. Körner, A coupled Cellular Automaton-Lattice Boltzmann model for grain structure simulation during additive manufacturing, *Comput. Mater. Sci.* 124 (2016) 37–48.
- [27] W.E. King, A.T. Anderson, R.M. Ferencz, N.E. Hodge, C. Kamath, S.A. Khairallah, A.M. Rubenchik, Laser powder bed fusion additive manufacturing of metals; physics, computational, and materials challenges, *Appl. Phys. Rev.* 2 (2015) 041304.
- [28] R. Rai, T.A. Palmer, J.W. Elmer, T. DebRoy, Heat transfer and fluid flow during electron beam welding of 304L stainless steel alloy, *Weld. J.* 88 (2009).
- [29] R. Martukanitz, P. Michaleris, T. Palmer, T. DebRoy, Z.-K. Liu, R. Otis, T.W. Heo, L.-Q. Chen, Toward an integrated computational system for describing the additive manufacturing process for metallic materials, *Addit. Manuf.* 1–4 (2014) 52–63.
- [30] T.M. Rodgers, J.D. Madison, V. Tikare, M.C. Maguire, Predicting mesoscale microstructural evolution in electron beam welding, *JOM* 68 (2016) 1419–1426.
- [31] J. Irwin, E.W. Reutzel, P. Michaleris, J. Keist, A.R. Nassar, Predicting microstructure from thermal history during additive manufacturing for Ti-6Al-4V, *J. Manuf. Sci. Eng.* 138 (2016) 111007.
- [32] M.F. Ashby, K.E. Easterling, A first report on diagrams for grain growth in welds, *Acta Metall.* 30 (1982) 1969–1978.
- [33] J.C. Ion, K.E. Easterling, M.F. Ashby, A second report on diagrams of microstructure and hardness for heat-affected zones in welds, *Acta Metall.* 32 (1984) 1949–1962.
- [34] E.A. Holm, C.C. Battaile, The computer simulation of microstructural evolution, *JOM* 53 (2001) 20–23.
- [35] D.L. Olmsted, S.M. Foiles, E.A. Holm, Survey of computed grain boundary properties in face-centered cubic metals: I. Grain boundary energy, *Acta Mater.* 57 (2009) 3694–3703.
- [36] D.L. Olmsted, E.A. Holm, S.M. Foiles, Survey of computed grain boundary properties in face-centered cubic metals—II: Grain boundary mobility, *Acta Mater.* 57 (2009) 3704–3713.
- [37] A. Garcia, V. Tikare, E. Holm, Three-dimensional simulation of grain growth in a thermal gradient with non-uniform grain boundary mobility, *Scripta Mater.* 59 (2008) 661–664.
- [38] J. Goldak, M. Akhlaghi, *Computational Welding Mechanics*, first ed., Springer, New York, NY, 2005.
- [39] A.A. Antonyssamy, J. Meyer, P.B. Prangnell, Effect of build geometry on the β -grain structure and texture in additive manufacture of Ti6Al4V by selective electron beam melting, *Mater. Charact.* 84 (2013) 153–168.
- [40] E. Nishida, B. Song, M. Maguire, D. Adams, J. Carroll, J. Wise, J. Bishop, T. Palmer, in: *EPJ Web of Conferences*, 2015, p. 01001.
- [41] R.R. Dehoff, M.M. Kirka, W.J. Sames, H. Bilheux, A.S. Tremsin, L.E. Lowe, S.S. Babu, Site specific control of crystallographic grain orientation through electron beam additive manufacturing, *Mater. Sci. Technol.* 31 (2015) 931–938.
- [42] E. Cakmak, T.R. Watkins, J.R. Bunn, R.C. Cooper, P.A. Cornwell, Y. Wang, L.M. Sochalski-Kolbus, R.R. Dehoff, S.S. Babu, Mechanical characterization of an additively manufactured inconel 718 theta-shaped specimen, *Metall. Mater. Trans. A* 47 (2015) 971–980.
- [43] J.Y. Guédou, C. Körner, H. Helmer, A. Bauereiß, R.F. Singer, J. Choné, Tailoring the grain structure of IN718 during selective electron beam melting, *MATEC Web of Conferences*, vol. 14, 2014, p. 08001.
- [44] J. Schindelin, I. Arganda-Carreras, E. Frise, V. Kaynig, M. Longair, T. Pietzsch, S. Preibisch, C. Rueden, S. Saalfeld, B. Schmid, J.Y. Tinevez, D.J. White, V. Hartenstein, K. Eliceiri, P. Tomancak, A. Cardona, Fiji: an open-source platform for biological-image analysis, *Nat. Methods* 9 (2012) 676–682.
- [45] M.A. Groeber, M.A. Jackson, DREAM.3D: a digital representation environment for the analysis of microstructure in 3D, *Integr. Mater. Manuf. Innov.* 3 (2014).
- [46] J.E. Bishop, J.M. Emery, C.C. Battaile, D.J. Littlewood, A.J. Baines, Direct numerical simulations in solid mechanics for quantifying the macroscale effects of microstructure and material model-form error, *JOM* 68 (2016) 1427–1445.
- [47] J. Cao, F. Liu, X. Lin, C. Huang, J. Chen, W. Huang, Effect of overlap rate on recrystallization behaviors of Laser Solid Formed Inconel 718 superalloy, *Opt. Laser Technol.* 45 (2013) 228–235.
- [48] J.D. Madison, V. Tikare, E.A. Holm, A hybrid simulation methodology for modeling dynamic recrystallization in UO2 LWR nuclear fuels, *J. Nucl. Mater.* 425 (2012) 173–180.
- [49] A.A. Brown, L.A. Deibler, L.L. Beghini, T.D. Kostka, B.R. Antoun, Process modeling and experiments for forging and welding, in: B.R. Antoun (Ed.), *Proceedings of the 2015 Annual Conference on Experimental and Applied Mechanics, Challenges in Mechanics of Time Dependent Materials*, vol. 2: Springer International Publishing, 2016, pp. 19–25.
- [50] T. Vilario, C. Colin, J.D. Bartout, As-fabricated and heat-treated microstructures of the Ti-6Al-4V alloy processed by selective laser melting, *Metall. Mater. Trans. A* 42 (2011) 3190–3199.
- [51] G.P. Dinda, A.K. Dasgupta, J. Mazumder, Texture control during laser deposition of nickel-based superalloy, *Scripta Mater.* 67 (2012) 503–506.